Three-Dimensional Optical-Tomographic Localization of Changes in Absorption Coefficients in the Human Brain

Avraham Bluestone[a], Gassan Abdoulaev[a], Randall Barbour[a,b],
Christoph Schmitz[a], Andreas H. Hielscher[*a,b]

[a]Dept. of Pathology, State University of New York - Downstate Medical Center, Brooklyn, NY
[b]Dept. of Electrical and Computer Engineering, Polytechnic University, Brooklyn, NY

ABSTRACT

We report on the first three dimensional tomographic localization of vascular reactivity in the brain. Using a model-based iterative image reconstruction algorithm we show the spatial distribution of changes in the absorption coefficient caused by changes in blood volume. Unlike currently available topographic reconstruction techniques, three-dimensional, volumetric reconstruction schemes promise to be capable of spatially distinguishing between signals originating in the cerebral cortex from those originating in the overlying tissues.

Keywords: Diffuse optical tomography, brain imaging, three-dimensional imaging, inverse-problem.

1. INTRODUCTION

In recent years there has been an increased interest in using diffuse optical tomography (DOT) for imaging the brain.[1-12] It is well established that near-infrared light can be used to probe the brain for changes in blood oxygenation during functional neural activation or changes in blood volume as they occur in injuries like hematomas. In most of the currently established protocols, either a single source and a single detector is used to perform point measurements, or an array of sources and detectors with a fixed geometry is employed to obtain topographic maps. Topographic maps show spatially resolved changes in the absorption coefficient during certain exercise protocols, such as finger flexes or breath holds. These maps project the cortical response together with the superficial vascular changes onto a two-dimensional surface map. The resulting surface maps are usually obtained by back-projecting absorption coefficients along a line between source and detector pairs.[2] These absorption coefficients are obtained by fitting a light propagation model to the measured data.

The goal of this paper is to go beyond topographic maps and obtain volumetric reconstructions of the changes in optical properties inside the human head. The main advantage of using a volumetric imaging scheme is the ability to localize optical changes in 3-dimensional space and thereby possibly isolate cortical activity from more superficial phenomenon. Several components are required to perform three-dimensional optical tomographic reconstruction. First an instrument is needed that acquires high fidelity data sets. Second, the surface geometry and the locations of sources and detectors on this surface have to be determined with high accuracy. Third, an algorithm is required that allows for inclusion of arbitrary boundaries and provides an efficient way of volumetrically reconstructing changes of optical properties in the human head. In this study we describe these components and present the first 3-dimensional tomographic reconstruction of the changes in optical properties in the human forehead. As an example we have chosen a breath-hold experiment (Valsalva maneuver), for which we observed strong changes in the detected signal.

* ahielscher@downstate.edu; phone 718 270 4562; http://recon2.hscbklyn.edu; SUNY Downstate Medical Center, Dept. of Pathology, Box 25, 450 Clarkson Ave., Brooklyn, NY 11203.

Optical Tomography and Spectroscopy of Tissue IV, Britton Chance, Robert R. Alfano, Bruce J. Tromberg, Mamoru Tamura, Eva M. Sevick-Muraca, Editors, Proceedings of SPIE Vol. 4250 (2001)

2. METHODS

2.1 Instrumentation and Data Acquisition

Measurements on the human forehead are performed with the dynamic near-infrared optical tomography (DYNOT) instrument, which is currently under development in our laboratory.[13] This instrument operates in continuous-wave mode. A beam from a laser diode (wavelength λ = 800 nm) is sequentially coupled into different fiber bundles, which deliver the light to various positions on the human head. Each bundle has a diameter of 1 mm. Fast switching between different source positions is possible by means of an optical demultiplexer, which consists of a mirror that is rotated by a microprocessor-controlled brushless DC servomotor. A motion control unit allows up to ~50 start-stop motions per second. Each source fiber bundle forms one branch of a bifurcated fiber bundle that joins another branch, which has a diameter of 3-mm. This second branch is used for light detection. On the target surface, the fibers from the detector fiber bundle surround the fibers of the source fiber bundle in a bulls-eye geometry configuration. At the other end each detector fiber bundle terminates on a single silicon photodiode of a multi-channel detection module. This module incorporates analog signal conditioning hardware, such as adjustable gain stages to increase the dynamic range of detection, four lock-in amplifiers, and sample-and-hold circuits that improve signal quality and are necessary for timing purposes. The output voltages of the detector channels are measured by a data acquisition board and stored on a personal computer. The optical power sent to the target is about 10 mW. For the measurements presented in this work we used 8 sources and 8 detectors, resulting in 64 source-detector combinations. Five full tomographic data sets, involving all 64 source-detector pairs, were acquired per second. A more detailed description of the device can be found in Reference 13.

2.2 Determination of Surface Coordinates

For optical tomographic imaging reconstructions one has to determine with high accuracy the surface geometry of the object whose internal properties need to be calculated. Furthermore, the precise locations of the sources and detectors have to be known. To achieve this accuracy we employed the techniques of photogrammetry.[14,15] The basis of photogrammetry is triangulation. The 3-dimensional coordinates of an object's surface are calculated knowing the camera locations and angles between light rays from the object and the camera images' planes. To determine the 3-D coordinates of points on the surface of the head, each point of interest must appear in at least two photographs, which are taken from different angles. Since the human head does not possess an intrinsic set of easily identifiable target points, we explored three different techniques of placing defined grid patterns over the convex surface of the head. The goal was to find a simple yet accurate method that could be used routinely in a clinical setting.

In the first approach we generate a grid pattern on the skin by passing a low-power laser beam through a diffraction beam splitter. This method has the advantages of being contact free, of having reference points that are located directly on the skin, and of having the ability to deal with arbitrarily complex contours. We found that the disadvantages of this procedure are that it can produce motion artifact if the patient isn't immobilized, can only be applied to areas with thin hair, and requires dim lighting for sharp delineation of the crosshatches.

The second approach involves using a thermoplastic mesh. The mesh becomes malleable as the temperature is raised and can be custom fit to the shape of any body surface (e.g. www.thermoplastic.com). When the temperature returns to room temperature the mesh becomes rigid again. Figure 1a shows such a mesh fixed in place on the forehead of a subject. This approach has the advantage that electrodes can be embedded directly in the mesh, thereby securing the electrodes in place and preventing motion artifact. Also, the position of the electrodes and the surface geometry is preserved indefinitely allowing the photographing of the surface to be performed at a different time than the experiment. Disadvantages of this method are that it is not contact-free and that the reference points (i.e. surface information) are displaced from the surface of the head by the thickness of the thermoplastic. However, the last point is easily overcome, by translating all points along the surface normals by the thickness of the thermoplastic mesh.

In the third approach we simply place circular retro-reflective markers on the head, as seen in Figure 1b. These markers, because of their circular shape, have the advantage of allowing sub-pixel precision when used in combination with a centroid-locating algorithm. They can either be fastened to hair-free areas of the head or attached to the optodes themselves, thus allowing for the imaging of hair-dense areas. Disadvantages of this method are that placing the markers can be cumbersome and that many markers are needed when tightly curved structures are considered.

Other approaches, such as the use of holographic imaging or laser surface scanning devices, are also feasible. However, their technical complexity paired with their high costs make them less practical and appealing in a day-to-day clinical setting.

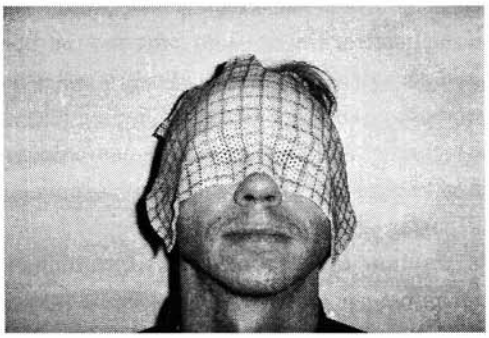

Fig. 1a: Thermoplastic mesh.

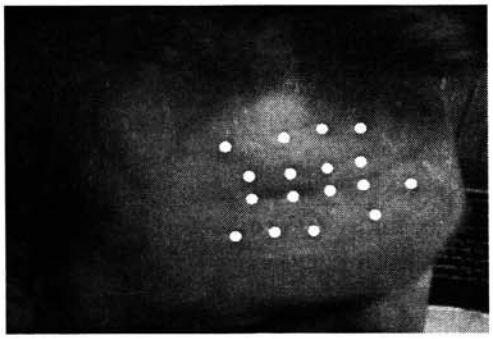

Fig. 1b: Retro-reflective stickers.

Once reference points are generated on the surface of the head, the area of interest is photographed from different angles with a digital camera (SONY Mavika FD-90). The camera needs to be calibrated for accurate determination of the surface coordinates from these photos. Effective focal length and possible optical aberrations are determined by photographing a well-defined square target with a known length, width, and distance from the camera.

These images of the head are then analyzed with a commercially available photogrammetry software package (Photomodeler, Eos Systems Inc., Vancouver, Canada). The analysis of the photographs proceeds in several steps. First, the location of the targets in each photograph must be marked. For the laser pattern, the targets are points of intersection of laser light; for the thermoplastic grid, the target points are the intersections of lines; and for the reflective stickers, the target points are their respective geometric centers. An edge-finding algorithm combined with a centroid-locating algorithm automatically determines these centers. The second step of the data analysis, termed referencing, is identifying which marked points are the same in all photographs. If a sufficient number of targets appear in overlapping photographs the software will automatically calculate the three spatial coordinates and three orientation angles for the camera as well as all marked and referenced target points. This processing, using the "bundle adjustment algorithm," will compute all 3D coordinates of all referenced points and estimate their measurement precision. A higher spatial accuracy of the resulting surface can be achieved by increasing the number of points used for referencing. Experimenting with various 3D models of known dimension (such as cubes, spheres, and head models) we determined that using the reflective marker technique with 4 markers per cm^2 on the human forehead enabled us to determine the surface coordinates within an accuracy better than 0.25 mm.

2.3 Mesh Generation

Having generated the surface coordinates of the human head, which represents the boundary of our domain, it was necessary to build the corresponding volume mesh. To this end, the coordinates of the surface points obtained using the photogrammetric approach are exported to a volumetric mesh generator. In this work we used the CAD-style volume generator software package (GID, CIMNE Inter. Center for Num. Methods, Barcelona, Spain). This package allows one to manually extend the surface in the z direction and build the corresponding volume mesh. Since computational time depends

on the number of mesh nodes, we limited the volume to a zone beneath the surface of interest, and not to the entire head. We typically chose a volume that included at least all areas with a fluence value eight orders of magnitude smaller than the source strength. We found that larger volumes are not necessary to consider for the reconstruction of optical properties in the head, because using larger volumes does not influence the reconstruction results. Figures 2a and 2b show an example of a surface and volume mesh, respectively, of a human forehead. The bridge of the nose is located at the black dot and the eyebrows are located to the left and right of this point.

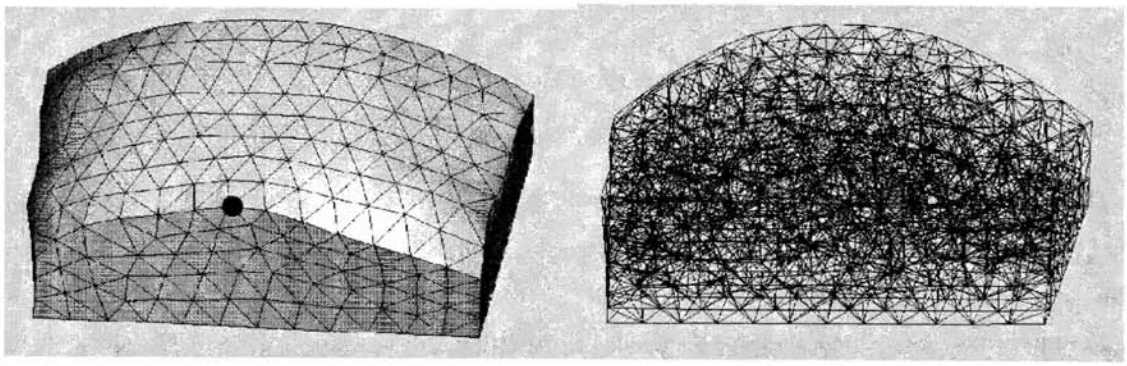

Fig. 2a: Surface mesh of forehead. Black dot indicates the bridge of the nose.

Fig. 2b: Volumetric mesh of forehead.

2.4 Image Reconstruction Algorithm

For the 3-dimensional reconstruction of the optical properties in the human head, we employ in this work a model-based iterative image reconstruction (MOBIIR) scheme.[16-19] A MOBIIR scheme consists, in general, of three major parts: (1) a forward model that predicts the detector readings based on a given spatial distribution of optical properties $\boldsymbol{\zeta} = (\mu_a(\mathbf{r}), D(\mathbf{r}))$, (2) an objective function Φ that compares predicted with measured signals, and (3) an updating scheme that uses the gradient of the objective function with respect to the optical properties to provide a means of updating the optical parameters for subsequent forward calculations.

The forward model, which we employ in this study, is the time-independent diffusion equation, given by

$$0 = \frac{\partial}{\partial x}\left(D\frac{\partial U}{\partial x}\right) + \frac{\partial}{\partial y}\left(D\frac{\partial U}{\partial y}\right) + \frac{\partial}{\partial z}\left(D\frac{\partial U}{\partial z}\right) - c\mu_a U + S \tag{1}$$

This partial differential equation is solved using a finite element forward solver based on the Galerkin weak form of Eq. 1.[20] We used Robin boundary conditions that take into account the refractive index mismatch between tissue and skin. The solver incorporates a Bramble-Pasciak-Xu (BPX) multi-grid preconditioner and an optimized conjugate gradient matrix solver, and allows for mesh refinement and multi-domain decomposition.[21]

Commonly the objective function is given by the mean-square error between predicted and measured data, P and M, respectively, where indices s and d refer to specific source and detector positions:

$$\Theta = \sum_s \sum_d \frac{\left(M_{s,d} - P_{s,d}(\boldsymbol{\zeta})\right)^2}{P_{s,d}(\boldsymbol{\zeta})} \tag{2}$$

In order to apply the objective function as defined by Eq. (2) towards image reconstruction, one needs to know the absolute measurement values M, which in many cases is difficult to obtain. On the other hand, most of the currently available measurement devices, including our DYNOT system, can provide, with high accuracy, relative measurements (M^{pert}/M^{ref}), where M^{pert} and M^{ref} are two different data sets acquired during a perturbation and reference state, respectively.[22,23] To accommodate the data type generated by our instrument we define a modified objective function given by

$$\Theta = \sum_s \sum_d \frac{\left(\frac{M_{s,d}^{pert}}{M_{s,d}^{ref}} P_{s,d}^0(\zeta_0) - P_{s,d}(\zeta) \right)^2}{P_{s,d}^2(\zeta)}. \tag{3}$$

Here the relative changes ($M_{s,d}^{pert} / M_{s,d}^{ref}$) are multiplied with the predicted detector readings $P^0_{s,d}$ obtained from an initial distribution ζ_0 of the optical properties (typically assumed to be homogeneous). In subsequent iterations a distribution ζ is sought, which produces the same predictions $P_{s,d}(\zeta)$ as $(M_{s,d}^{pert} / M_{s,d}^{ref}) * P_{s,d}^0$. The resulting distribution ζ is then a spatial representation of the differences in optical properties that led to the differences measured between M^{pert} and M^{ref}.

To update the initial distribution of optical properties, one must calculate the gradient of the objective function with respect to all optical properties. The calculation of the gradient was performed using the technique of adjoint differentiation as described in previous publications.[18,24,25] The gradient defines a "direction" along which a line minimization is performed. Once the line minimization is completed a new gradient is calculated and a new direction for the line minimization is found within a multidimensional conjugate gradient descent algorithm.[16] Typically 20-30 iterations with different gradients are necessary before the algorithm converges.

2.5 Experimental Protocol

The experiment was designed to look at functional hemodynamic changes in the forehead of a single patient induced by a breath hold (Valsalva maneuver). For the measurement the patient was placed in the supine position and a two-tiered band was used to secure 8 optodes to the right forehead, as per insert of figure 3. Each optode consisted of a co-located source and detector, and all measurements were performed at a wavelength of λ = 800 nm. This wavelength is the isosbestic point of oxy- and deoxy-hemoglobin and therefore any changes in signal reflect blood volume changes only. The time series consisted of 2000 images, which were acquired at a rate of 5Hz. The first 200 images were taken during a rest period, in which the subject breathed normally. This was followed by a 40-second-long period of deep breathing. Then the subject performed a breath-hold, which was held for as long as possible and then released. During the remainder of the time series the arms and legs of the patient were raised and lowered by a technician. These manipulations lead to a redistribution of blood in the body. It should be noted that signal changes during this period are not caused by motion artifacts, since the head remained immobilized during the movement of the extremities. Also, prior to any experimental protocols we asked the patient to move his head from side to side to record the baseline motion artifact. Only after these artifacts were minimized was the protocol performed.

3. RESULTS

A representative trace of the measured output produced by the DYNOT system for the experimental protocol is shown in Fig. 3. The location of the eight co-located sources and detectors on the right forehead are shown in the inset of Fig. 3. The source-detector patch covers a 2cmx3cm area. Figure 3 displays eight traces of the measured intensity during various activities for source position number one.

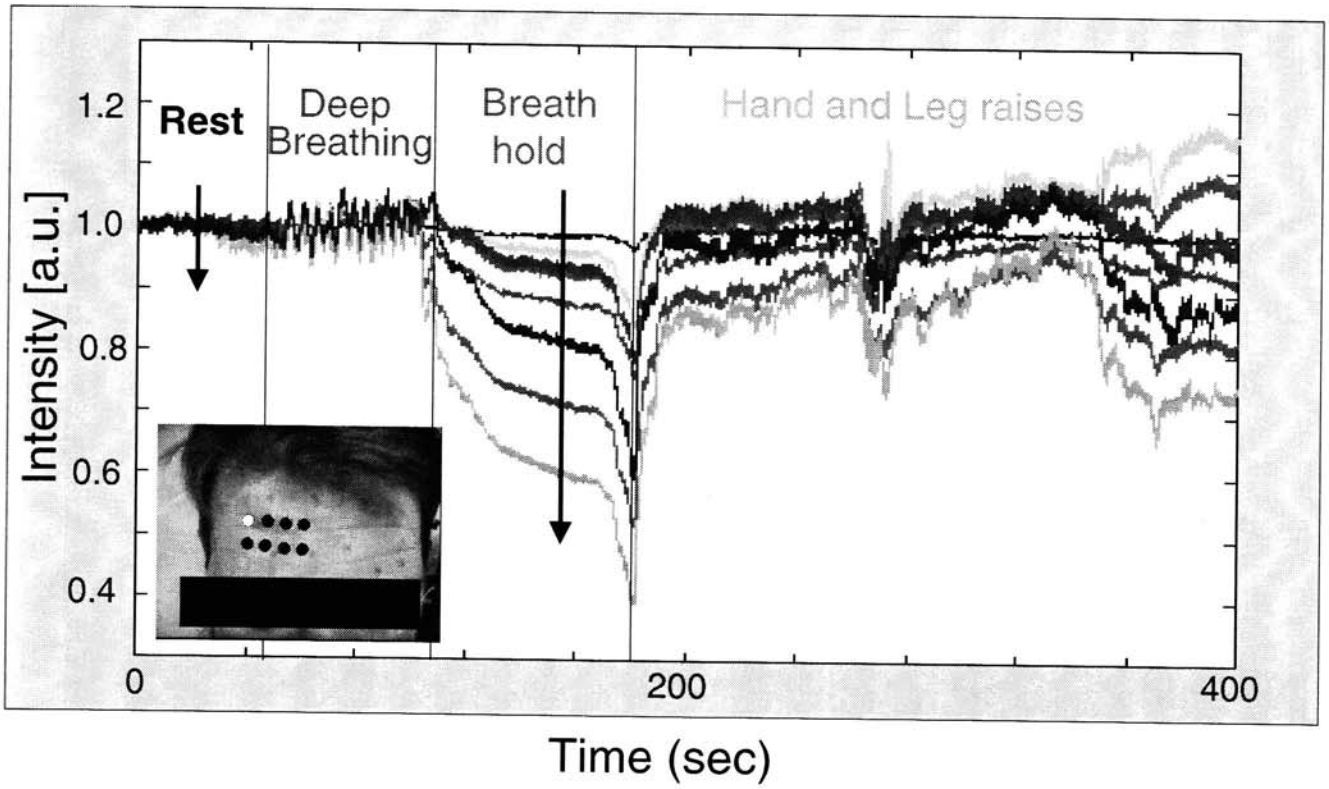

Fig. 3: Time series of the experimental protocol. The inset shows the source-detector arrangement on the forehead. The source position is indicated by a white circle, while detector position are shown by black circles.

As can be seen during the rest period the measurements are very stable and fluctuate by less than 1%. With the onset of deep breathing a cyclic pattern appears with changes of up to 5%. During the following breath-hold the measured signals drop by up to 60% for the detector furthest from the source. (For other source detector combinations, increases for certain detectors could also be observed.) Once the breath hold is released the signal approaches signal levels seen during rest. Arm and leg raises performed towards the end of the experiment lead to changes in vascular perfusion which are visible as changes in the optical signal.

For the difference reconstruction, using the objective function in Eq. 3, we used the ratio of the two arrows seen in Fig. 3. These arrows represent a time point for all source/detector combinations during rest and during a breath-hold. Figure 4 consists of three volumetric reconstruction views, as well as a cut in the horizontal plane in the midline of the forehead after 50 iterations that took 3 hours on a Pentium III 550Mhz processor. Displayed in figures 4a-c are volumes (isosurfaces) in which the absorption coefficient is increased by more than 15% or decreased by more than 20%, respectively. The area with a decreased absorption coefficient is located between the two areas that show an increase in the absorption coefficient (Fig. 4a, 4b). The decreased portion is located slightly deeper inside the head (~ 1.7 cm) than the increased absorption, which is closer to the surface (~1.4cm) (Fig 4c).

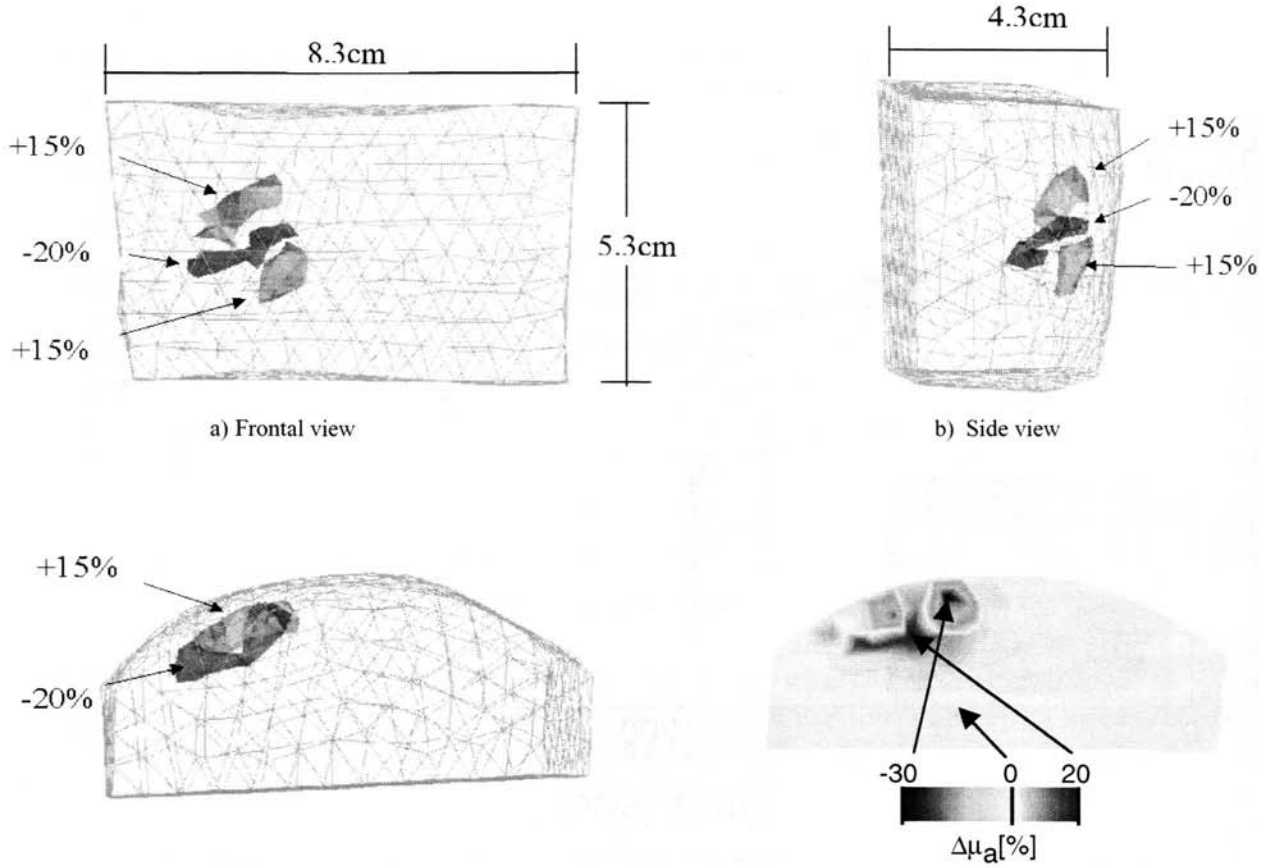

a) Frontal view

b) Side view

c) Horizontal view

d) Horizontal slice through midline forehead

Fig 4a-d: Three-dimensional reconstruction of changes in the absorption coefficient during breath-hold experiments. The different gray regions indicate areas with 15% increase and 20% decrease in μ_a, respectively.

4. DISCUSSIONS

4.1 Physiological Interpretation

In order to interpret the physiological change seen in Fig. 4, it is necessary to understand the physiology of a breath-hold (Valsalva maneuver). The Valsalva maneuver, a forced expiration against a closed glottis, increases intrathoracic pressure and affects heart rate and blood pressure. As intrathoracic pressure rises to extremely high levels, this pressure abruptly limits venous return. Next, the decreased venous return reduces left ventricular output and decreases arterial blood volume. Following release of the Valsalva maneuver, there is a marked overshoot of blood pressure and cardiac output. The right frontal area of the head contains two main arterial distributions: one provided by the anterior and middle cerebral arteries, and one (more superficially) provided by the anterior meningeal artery. The anterior and middle cerebral arteries, which arise from the internal carotid, supply the frontal cortical lobes medially and laterally, respectively. The anterior meningeal artery, which arises from branches of the external carotid artery (anterior and posterior ethmoidal arteries), supplies the intracranial dura (meninges).

The main venous distribution consists of superficial cerebral veins, which lie along the surface sulci, below the skull. During a Valsalva maneuver one would expect an increased blood volume in these veins and a decreased blood volume in the surrounding arteries overlying that area. However, because of the tight regulation of blood flow in the head, this effect

should be more pronounced in the superficial areas. Since the reconstruction (Fig. 4a-d) reflects only blood volume changes, it is difficult to assert if the increase and decrease in μ_a reflect venous or arterial blood respectively; it does, however, allow us to show not only that a redistribution of volume does occur, but also that it appears to be localized 1.5 cm from the surface.

4.2 Spatial Localization

The question arises of how accurate is the depth localization of the absorption changes, given that data from only a small arc over the location of interest is available? To investigate this question we performed synthetic simulations on the same human forehead mesh described above.

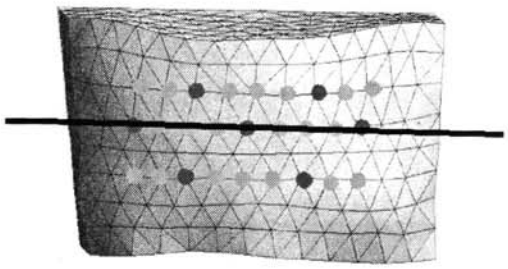

Fig 5a: Source detector placement and location of transverse sections (thick black line).

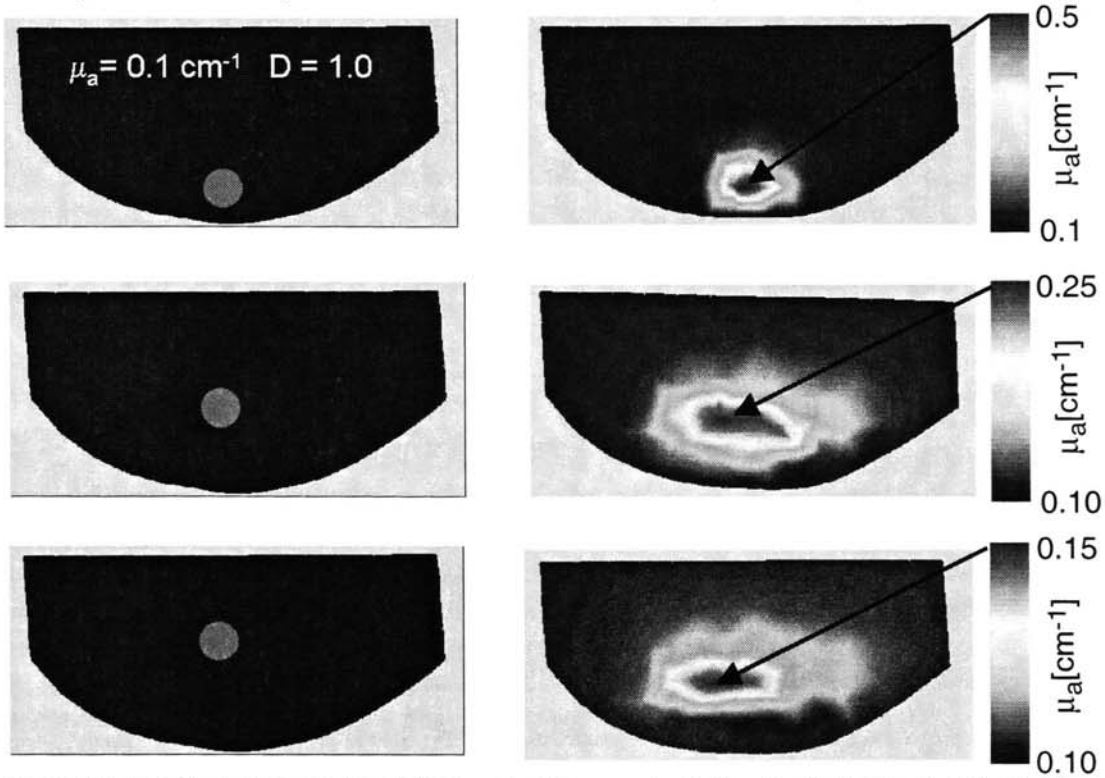

Fig. 5b: Location of actual perturbations (left column) and the reconstructed location (right column). Notice that the grayscales cover a different range of optical properties for all three reconstructed images.

In the simulation we placed seven sources and 29 detectors on the outer surface of the forehead (Fig. 5a). A one-centimeter spherical object (representing a hematoma) with a μ_a value of $0.5cm^{-1}$ was imbedded in the para-sagital plane of the forehead at distances of .7cm, 1.7cm, and 2.6 cm from the surface. Starting with an initial guess of $0.1cm^{-1}$ for the background μ_a, the positions of the resultant reconstruction series can be seen in Fig 5b. Two observations are apparent. First, the deeper imbedded the object the more diffuse the reconstruction appears. Second, the difference between the actual and reconstructed location increases with increasing depth of the object. We repeated these reconstructions using μ_a values for the object of $0.2cm^{-1}$ and $1.0cm^{-1}$, and in all cases observed the same phenomenon. In Fig. 6, we have plotted the apparent depth (reconstructed) versus the actual depth (true location). The apparent depth of the object from the surface is defined as the location with the highest absorption coefficient in the reconstructed image. In the ideal case one would expect the reconstructed depth to follow the main diagonal (Fig. 6 Ideal). However, the curves for all three μ_a values begin to deviate from this ideal line at a depth of 0.7cm; as the depth of the object is increased the deviation from the ideal line gets stronger. It is noteworthy that this effect seems to be independent of the strength of the perturber. Therefore, it may be possible to correct for this phenomena, by including an appropriate spatial regularization scheme into the reconstruction scheme. Given the results of this numerical study we can estimate that the areas of increased and decreased absorption, observed during the breath-hold experiment, are most likely located deeper inside the head than 1.5 cm.

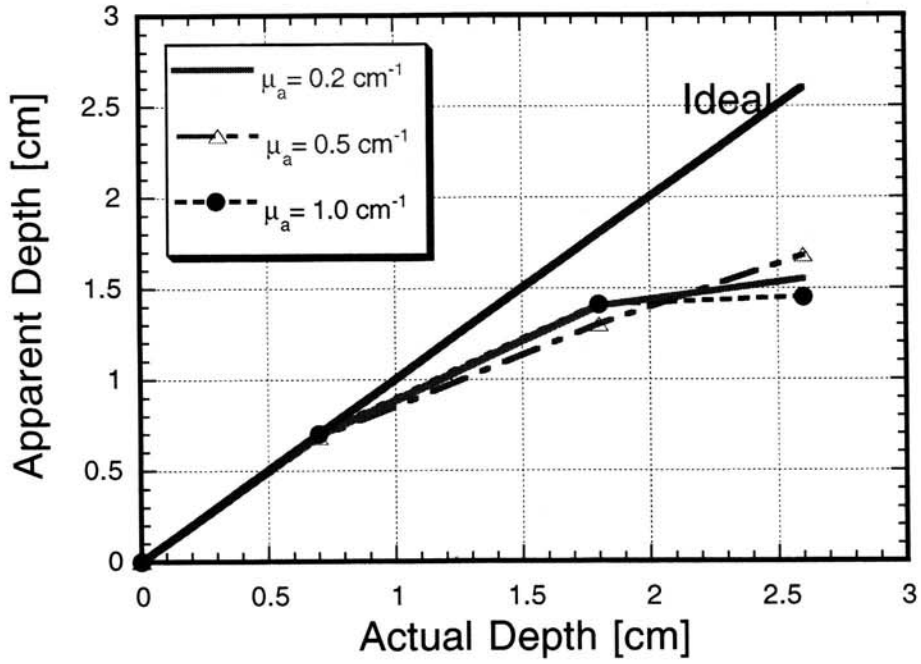

Fig. 6: Reconstructed locations of a spherical heterogeneity with 3 different values of μ_a at three different distances from the surface. In the ideal case the apparent (reconstructed) depth would be the same as the actual depth (solid black line).

5. SUMMARY

In this paper we have reported on the first volumetric reconstructions of the optical properties in the forehead during a breath-hold using a 3-dimensional model-based iterative image reconstruction scheme. We placed a two-tiered band with 8 sources and detectors over a patient's right frontal forehead. The source-detector patch covered an area of 2x3 cm^2. Using photogrammetric techniques we determined the surface coordinates of both the head section, and the location of our probes. These coordinates were exported to a finite element mesh generator, which we used to construct a subsurface volume of the

head region. This information together with measurement data performed on the forehead became input to our model-based iterative image reconstruction scheme. This scheme used a diffusion-based finite-element solver to predict measurements on the forehead given source-detector position and optical properties inside the head. As the objective function we employed a modified least-square error norm, which allowed using relative measurement data. Starting from an initial guess the optical properties were updated by a conjugate gradient search algorithm that uses the adjoint differentiation method for obtaining the gradient. Using this code we volumetrically reconstructed areas of change in the optical properties in the human forehead during a breath-hold (Valsalva maneuver) experiment. The observed changes are consistent with the expected physiological changes seen during the Valsalva maneuver. However, more studies involving multiple wavelengths and the incorporation of spatial regularization schemes will be necessary to fully explore the potential of volumetric brain reconstructions.

ACKNOWLEDGEMENTS

This work was supported in part by the City of New York Council Speaker's Fund for Biomedical Research: Toward the Science of Patient Care and the National Institutes of Health (grant # 2R44-HL-61057-02A1), and by the Dean's Office of the College of Medicine at the State University of New York (SUNY) Downstate Medical Center in Brooklyn, NY.

REFERENCES

[1] D. A. Benaron, S. R. Hintz, A. Villringer, D. Boas, A. Kleinschmidt, J. Frahm, C. Hirth, H. Obrig, J. C. Van Houten, E. L. Kermit, W. Cheong, D. K. Stevenson, "Noninvasive functional imaging of human brain using light", J. Cerebral Blood Flow and Metabolism, **20**, pp. 469-477, 2000.

[2] M. Franceschini, V. Toronov, M. E. Filiaci, E. Gratton, S. Fantini, "On-line optical imaging of the human brain with 160-ms temporal resolution", Optics Express, **6**(3), pp. 49-57, 2000.

[3] S. Fantini, D. Huebert, M. A. Franceschini, E. Gratton, W. Rosenfeld, P. G. Stubblefield, D. Maulik, and M. Stankovic, "Non-invasive optical monitoring of the newborn piglet brain using continuous-wave and frequency-domain spectroscopy", Phys. Med. Biol., **44**, pp. 1543-1563, 1999.

[4] M. R. Stankovic , D. Maulik, W. Rosenfeld, P. G. Stubblefield, A. D. Kofinas, S. Drexler, R. Nair, M. A. Franceschini, D. Hueber, E. Gratton, and S. Fantini,, "Real-time optical imaging of experimental brain ischemia and hemorrhage in neonatal piglets", J. Perinat. Med., **27**, pp. 279-286, 1999.

[5] H. Koizumi, Y. Yamashita, A. Maki, T. Yamamoto, Y. Ito, H. Itagaki, and R. Kennan, "Higher-Order Brain Function Analysis by trans-cranial dynamic near-infrared spectroscopy imaging", Journal of Biomedical Optics. **4**(4), pp. 403-413, 1999.

[6] A. Villringer and B. Chance, "Non-invasive optical spectroscopy and imaging of human brain function", Trends Neuroscience, **20**(10), pp. 435-442, 1997.

[7] M. Tamura, Y. Hoshi, and F. Okada, "Localized near-infrared spectroscopy and functional optical imaging of brain activity," Philosophical Transactions of the Royal Society of London - Series B: Biological Sciences, **352**(1354), 737-42, 1997.

[8] A. Kleinschmidt, Hellmuth Obrig, M. Requardt, K. Merboldt, U. Dirnagl, A. Villringer, and J. Frahm, "Simultaneous recording of cerebral blood oxygenation changes during human brain activation by magnetic resonance imaging and near infrared spectroscopy", J. of Cerebral blood flow and metabolism, **16**(5), pp. 817-826, 1996.

[9] H. Liu, B. Chance, A. H. Hielscher, S. L. Jacques, F. K. Tittel, "Influence of blood vessels on the measurement of hemoglobin oxygenation as determined by time-resolved reflectance spectroscopy", Medical Physics, **22**(8), pp. 1209-1217, 1995.

[10] G. Gratton and M. Fabiani, "Dynamic brain imaging: Event-related optical signal (EROS) measures of the time course and localization of cognitive-related activity", Psychonomic Bulletin and Review, **5**(4), pp. 535-563, 1995.

[11] A. Maki, Y. Yamashita, Y. Ito, E. Watanabe, Y. Mayanagi, H. Koizumi, "Spatial and temporal analysis of human motor activity using non-invasive NIR topography", J. Med. Phys. **22**(12), pp. 1997-2005, 1995.

[12] Y. Hoshi and M. Tamura, "Detection of dynamic changes in cerebral oxygenation coupled to neuronal function during mental work in man", Neuroscience Letters, **150**, pp. 5-8, 1993.

[13] C.H. Schmitz, M. Löcker, J. Lasker, A.H. Hielscher, R.L. Barbour, "Performance characteristics of a silicon-photodiode-based instrument for fast functional optical tomography," in *Optical Tomography and Spectroscopy of Tissue IV*, B. Chance, R.R. Alfano, B.J. Tromberg, M Tamura, and E.M. Sevick, eds., Proceedings of SPIE Vol. 4250, Bellingham, WA, 2001 (in press).

[14] H. M. Karara, *Handbook of Non-topographic Photogrammetry*, American Society of Photogrammetry, Falls Church, VA, 1989.

[15] E. F. Church, *Elements of Photogrammetry*, Syracuse University Press, New York, 1948.

[16] A. H. Hielscher, A. D. Klose, K. M. Hanson, "Gradient-based iterative image reconstruction scheme for time-resolved optical tomography", IEEE Trans Med Imag., **18**(3), pp. 262-271, 1999.

[17] A. D. Klose, and A. H. Hielscher, "Iterative reconstruction scheme for optical tomography based on the equation of radiative transfer", *Medical Physics,* **26** (8), pp. 1698-1707, 1999.

[18] R. Roy and E. M. Sevick-Muraca, "Truncated Newton's optimization scheme for absorption and fluorescence optical tomography: Part I Theory and formulation", Optics Express **4**(10), 353-371, 1999.

[19] S. R. Arridge, M. Schweiger, "A gradient-based optimization scheme for optical tomography", Optics Express **2** (6), pp. 213-226, 1998.

[20] G. Abdoulaev, A. Varone and G. Zanetti, "An object oriented flow solver for the CRS4 virtual vascular project", in Proceedings of the 3rd European conference on Numerical mathematics and advanced applications, World Scientific, Singapore, pp. 407-415, 2000.

[21] J. H. Bramble, J. E. Pasciak, and J. Xu, "Parallel multilevel preconditioners", Math. Comp. **55**, pp. 1-22, 1990.

[22] Y. Pei, *Optical tomographic imaging using the finite element method*, Ph.D. Thesis, Polytechnic University, Brooklyn, NY, 1999.

[23] Y. Pei, H.L. Graber, R.L. Barbour, "Normalized-constrained method for minimizing inter-parameter cross-talk in reconstructed images of spatially heterogeneous scattering and absorption coefficients," in *Optical Tomography and Spectroscopy of Tissue IV*, B. Chance, R.R. Alfano, B.J. Tromberg, M Tamura, and E.M. Sevick, eds., Proceedings of SPIE Vol. 4250, Bellingham, WA, 2001 (in press).

[24] A. J. Davies, D. B. Christianson, L. C. W. Dixon, R. Roy, and P. van der Zee, "Reverse differentiation and the inverse diffusion problem", Advances in Engineering Software, **28**, pp. 217-221, 1997.

[25] D.B. Christianson , A. J. Davies, L. C. W. Dixon, R. Roy, P. Van der zee, "Giving Reverse Differentiation a Helping Hand", Optimization Methods and Software, **8**: 53-67, 1997.